J. Fluid Mech. (2019), *vol.* 880, *pp.* 497–513.

doi:10.1017/jfm.2019.731

Laser-induced forward transfer of viscoplastic fluids

Maziyar Jalaal[1,†], Martin Klein Schaarsberg[1], Claas-Willem Visser[2] and Detlef Lohse[1,3]

[1]Physics of Fluids Group, Max Planck Center for Complex Fluid Dynamics, MESA+ Institute and J.M. Burgers Centre for Fluid Dynamics, University of Twente, P.O. Box 217, 7500 AE Enschede, The Netherlands

[2]Thermal and Fluid Engineering Department, University of Twente, Enschede, P.O. Box 217, 7500 AE Enschede, The Netherlands

[3]Max Planck Institute for Dynamics and Self-Organisation, 37077 Göttingen, Germany

(Received 8 January 2019; revised 23 April 2019; accepted 31 August 2019; first published online 9 October 2019)

Laser-induced forward transfer (LIFT) is a nozzle-free printing technology that can be used for two- and three-dimensional printing. In LIFT, a laser pulse creates an impulse inside a thin film of material that results in the formation of a liquid jet. We experimentally study LIFT of viscoplastic materials by visualizing the process of jetting with high-speed imaging. The shape of the jet depends on the laser energy, focal height, surface tension and material rheology. We theoretically identify the characteristic jetting velocity and how it depends on the control parameters, and define non-dimensional groups to classify the regimes of jetting. Based on the results, we propose the optimal conditions for printing with LIFT technology.

Key words: complex fluids, non-Newtonian flows, interfacial flows (free surface)

1. Introduction

Laser-induced forward transfer (LIFT) is a direct-write method of printing. LIFT exploits the energy of a laser (continuous or pulsed) to locally transfer material from one surface to another. The various materials, such as metals (Pohl *et al.* 2015; Visser *et al.* 2015; Zenou, Sa'ar & Kotler 2015), pastes (Wang *et al.* 2010; Munoz-Martin *et al.* 2016) or liquids (Colina *et al.* 2006), are initially deposited on a transparent surface (the donor). The laser passes through this substrate and is absorbed by the material. Given large enough laser energy, a small part of the material is ejected and jetted towards the receiver substrate. Repeating the process, and moving the donor and the receiver, leads to two-dimensional (2-D) or three-dimensional (3-D) printing of a structure. A LIFT configuration can feature a metallic or polymeric dynamic release layer (DRL) between the transparent substrate and the material (Turkoz, Fardel & Arnold 2018*a*). A DRL absorbs the majority of the laser energy and provides

†Email addresses for correspondence: m.jalaal@utwente.nl, mazi@alumni.ubc.ca

momentum for the jetted material. LIFT is non-lithographic, nozzle-free and does not require a cleanroom for fabrication. For an overview of the research on LIFT, we refer the reader to the recent comprehensive review of Serra & Piqué (2018) and references therein.

The majority of LIFT studies up to now have focused on Newtonian liquids. However, a wide range of applications are based on complex materials, such as hydrogels in 3-D bio-printers (Xiong *et al.* 2015) and metallic pastes in electronic printing devices (Wang *et al.* 2010; Munoz-Martin *et al.* 2016). Very recently, Turkoz *et al.* (2018*b*) have studied LIFT of shear-thinning and viscoelastic jets. They used xanthan gum solutions of different concentrations in a LIFT system with a DRL and categorized the jet morphologies, identifying (modified) Deborah and Ohnesorge numbers as control parameters. They show that these non-dimensional groups span a phase space, with a no-droplet regime, a jetting regime and a fragmentation regime.

In the present work, we study LIFT of viscoplastic (VP) fluids. The main feature of such a material is the yield stress. Below this critical stress, the material behaves like an elastic solid. If the applied stress exceeds the yield stress, the material flows like a viscous fluid, typically featuring a nonlinear shear-dependent viscosity. For more information on VP fluids, see the reviews of Balmforth, Frigaard & Ovarlez (2014) and Bonn *et al.* (2017).

The paper is organized as follows. In § 2, we provide information on the experimental conditions, including the materials and the set-up. In § 3, we present the phenomenology and report on our high-speed observations of the regimes of jetting. In § 4, we will then theoretically derive the jetting velocity and present a dimensional analysis, identifying the non-dimensional groups governing the process. Finally, § 5 concludes the results and gives an outlook.

2. Experiments

2.1. *Materials*

For the experiments, we use mixtures of commercial hair gel from Europrofit and milli-Q water. The material is mainly a pH-neutralized aqueous solution of Carbopol (with triethanolamine). The material also includes a small amount of additional polymers (polyvinylpyrrolidone (PVP) and propyleneglycol) and features elastoviscoplastic properties (see Dinkgreve *et al.* 2016). We use an MCR 502 Anton-Paar rheometer with a cone-and-plate configuration to characterize the material properties. To avoid slip (see Roberts & Barnes (2001) and also Meeker, Bonnecaze & Cloitre (2004), Jalaal, Balmforth & Stoeber (2015)), we use sand-blasted surfaces with a roughness length scale of 4.2 ± 0.3 μm. The roughness size is close to the characteristic length of the microstructures of the solutions, being the diameter of the soft blobs of the polymers (see e.g. Kim *et al.* 2003; Géraud *et al.* 2017). We first perform oscillatory tests for a stress range of 0.03 Pa $\lesssim \tau \lesssim$ 100 Pa. Figure 1(*a*) shows the values of the elastic storage modulus G' and of the loss modulus G'' both versus the stress τ at an operating frequency of 1 Hz. At low stresses, the material is predominantly elastic ($G' \gtrsim 10G''$). The elastic moduli, however, decrease significantly at high stresses (when stress exceeds the yield stress), while the loss modulus becomes larger than the storage modulus.

We perform shear-rate-controlled tests to measure the viscous properties above the yield stress. The protocol was as follows: After placing the sample on the plate, we first pre-shear by ramping up the shear rate ($\dot{\gamma}$) from 0.01 s^{-1} to 500 s^{-1}. We then decreased the shear rate for the same range. The data were recorded during this

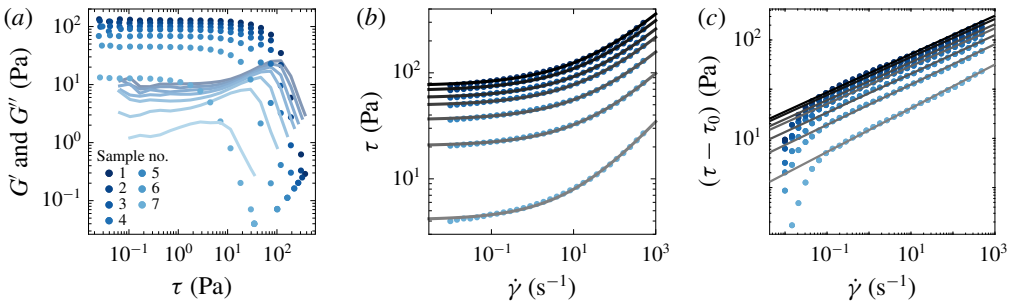

FIGURE 1. (Colour online) Rheology of the seven viscoplastic fluids analysed. Symbols and numbers refer to the different samples, whose material properties are given in table 1. (*a*) Storage modulus G' (symbols) and loss modulus G'' (lines) as functions of stress. (*b*) Flow curves: symbols are the experimental data and lines are the Herschel–Bulkley fits. (*c*) Viscous stress $\tau - \tau_0$ versus the shear rate (symbols) and their corresponding Herschel–Bulkley fits (lines).

decreasing shear-rate ramp. Note that a subsequent increasing shear-rate sweep test resulted in the same reported flow curve. Each data point is an average value over 10 s. The changes in the flow curves were negligible for waiting times longer than 10 s – in contrast to some other yield-stress fluids that require much longer waiting time (see e.g. Jalaal *et al.* 2017; Hopkins & de Bruyn 2019). Figure 1(*b*) shows the flow curves of the used material. The flow curves approach a plateau when $\dot{\gamma} \to 0$, i.e. the stress approaches the yield stress τ_0 and the apparent viscosity blows up. We quantify the properties of the materials using the following constitutive model:

$$\tau = \gamma G_0' \quad \text{if} \quad \tau < \tau_0, \quad \text{otherwise} \quad \tau = \tau_0 + K\dot{\gamma}^n, \tag{2.1}$$

where we assume that the material is a simple linear elastic solid below the yield stress (G_0' being the storage modulus at a small deformation limit) and a Herschel–Bulkley fluid above it. Using such a constitutive law, we ignore the viscous effects below the yield stress as well as elastic effects above the yield stress (viscoelasticity). We will later comment on the elastic effects in appendix B.

In (2.1), K and n are the consistency and flow indices, respectively. We find these values by directly fitting the flow-curve data (solid lines in figure 1*b*). To show the quality of the fits, we also plot the variation of the viscous stresses $(\tau - \tau_0)$ with $\dot{\gamma}$ in figure 1(*c*) (see Katgert *et al.* 2009; Lidon, Villa & Manneville 2017). We note that our fits, although satisfactory for $\dot{\gamma} > 0.1$ s^{-1}, include some error for small values of $\dot{\gamma}$. Alternatively, one can fit a linear curve to $\ln(\tau - \tau_0)$ versus $\ln(\dot{\gamma})$ with initially guessing and then searching for a yield stress that minimizes the error residuals (see appendix A in Katgert *et al.* (2009)). Such a method results in slightly larger values of the yield stress within the range of measurement errors (∼5 %). Table 1 lists the final coefficients for the samples used in our experiments. The rheological properties of our samples are similar to those reported for 0.1 %–1.5 % mass concentration of Ultrez 10 Carbopol in water (Dinkgreve *et al.* 2016). For increasing polymer concentration, the elastic modulus and the yield stress increase, i.e. the gel becomes stiffer. Table 1 also lists the values of the yield stress from the stress sweep tests, where G' and G'' intersect (another way to measure the yield stress). The yield-stress values from the intersection of the elastic moduli curves in the stress sweep tests are larger than those

Sample	τ_0 (Pa) – HB fits	τ_0 (Pa) – SS	K (Pa s^n)	n	G_0' (Pa)
1	75.3	138.9	20.2	0.38	110
2	67.7	123.7	17.6	0.38	101
3	57.7	100.0	14.2	0.38	94
4	49.1	84.0	11.6	0.39	86
5	35.9	60.5	8.01	0.39	71
6	20.5	34.5	4.67	0.41	60
7	4.1	7.5	1.39	0.45	42

TABLE 1. Values of yield stress τ_0 from the Herschel–Bulkley (HB) fits and from the intersection of G' and G'' in stress sweep (SS) tests, consistency index K, flow index n and storage modulus $\mathcal{G}_0'$, from (2.1).

found by the Herschel–Bulkley fits as also reported in Dinkgreve *et al.* (2016). In the text, we use the values obtained by the Herschel–Bulkley fit as that finds the most accurate values of yield stress (see the discussion in Dinkgreve *et al.* (2016)).

Measuring the surface tension of yield-stress materials is known to be challenging. The classic methods such as capillary rise or pendant drop methods fail when the yield stress is high enough to govern the interface shape (see Boujlel & Coussot 2013; Jørgensen *et al.* 2015). Nonetheless, the values of surface tension reported for (different types of) Carbopol in the literature (Hu, Wang & Hartnett 1991; Ishiguro & Hartnett 1992; Manglik, Wasekar & Zhang 2001; Boujlel & Coussot 2013; Jørgensen *et al.* 2015) show only small deviations from that of water. We hence use the standard value for water at 20 °C, $\sigma = 0.072$ N m^{-1}. Note that we could only measure the surface tension at very low gel concentrations (using a pendant drop method), where $\sigma = 0.069 \pm 0.02$ N m^{-1} was obtained. The slightly smaller values could be due to the presence of the other polymers inside the hair gel, which might even result in smaller surface tension values at higher gel concentrations. Therefore, the value of 0.072 N m^{-1} should be taken as an upper bound for the real surface tensions of our samples. The density of the gels is just slightly (∼0.2 %) larger than that of water (measured using a DMA-35 Anton-Paar density meter).

2.2. *Experimental set-up and parameters*

Figure 2 shows a schematic of our experimental set-up. We trigger a pulsed green Nd:YAG laser (Litron Nano S65-15PIV) with a delay generator (BNC Model 575). The emitted laser beam has a diameter of 4 mm, a pulse duration of $t_p = 6$ ns and a wavelength of $\lambda = 532$ nm. We control the energy of the laser (0.5 mJ $< E <$ 6.5 mJ) with a $\lambda/2$ wave plate, a polarizing beam splitter (PBS) and a beam dump (BD). We measure the pulse energy for every single experiment using a Gentec QE8SP-B-BL energy meter (EM). Note that, using a second energy meter (Gentec QE12LP-H-MB), we found the calibration relationship between the energy of the pulse inside the film and those measured. The laser pulse passes through a 10× objective (Thorlabs LMH-10X-532) and is focused inside the gel layer. Using a Gaussian beam approximation we find a spot size diameter of 3.4 μm. To form the gel layers, we use spacers of given height and flatten a previously deposited blob of the material, using a blade with a thickness of $H = 1$ mm (see figure 2*b*). The substrate is a glass slide clipped into a motorized 2-D stage. The yield stress of the materials prevents further spreading of the liquids. We can adjust the vertical position of the objective lens with a motorized

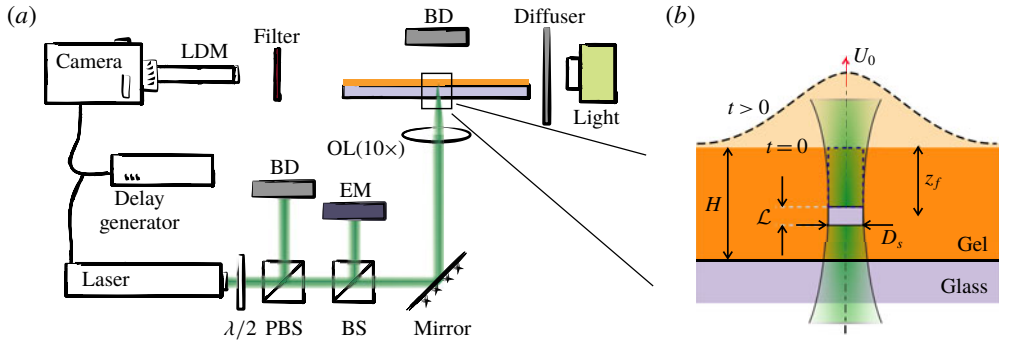

FIGURE 2. (Colour online) (*a*) Experimental set-up for the investigation of LIFT of viscoplastic materials (dimensions are not to scale). A laser pulse passes through a $\lambda/2$ plate and a polarizing beam splitter (PBS), which serve to control the beam energy. We measure the energy of the laser with an energy meter (EM). The laser is guided through a 10× objective lens (OL) and focused on a specified focal position. The side view is imaged with a high-speed camera attached to a long-distance microscope (LDM). The test section is illuminated through backlighting. The camera is protected with a notch filter. In the schematic, BD is the beam dump. (*b*) Magnified view of the test section. The grey part with thickness $\mathcal{L}$ is the cavity at the focal height z_f; D_s is the spot size; and the dashed line shows the deformed interface with a characteristic early velocity of U_0.

stage, to control the focal spot z_f. The side views are imaged with a high-speed camera (Photron FASTCAM SA-X2) attached to a long-distance microscope (Navitar 12X). The imaging is performed at a frame rate of 100 000 frames per second and a resolution of 17.8 μm per pixel. The illumination uses a collimated white light source (Sumita LS-M352A), passing through a diffuser. The set-up also utilizes a low-power continuous red laser for alignment and calibration of the vertical position (not shown here). The control parameters are the focal height z_f, the laser energy E and the rheological properties, e.g. the yield stress τ_0.

3. Phenomenology

In this section, we first report on the phenomenological behaviour of the jetting process for the variation of each control parameter and then classify the morphological changes with the help of the relevant non-dimensional groups. Figure 3(*a*) shows the process of jet formation for different laser energies for sample 5 and $z_f/H = 0.5$. Since we do not add any absorbing dye to our material, the gel layer is transparent to the laser. Therefore, we only see the jet formation when the laser fluence is above the optical breakdown threshold, $I = I_p \approx 1.3 \times 10^8$ J m^{-2}. This experimentally measured value is close to the previously reported breakdown threshold for water (Vogel *et al.* 1996; Kennedy, Hammer & Rockwell 1997) and remains the same for all the solutions, regardless of the polymer concentration. Above the optical threshold, plasma forms and a bubble starts to grow (Vogel *et al.* 1996; Ando, Liu & Ohl 2012; Obreschkow *et al.* 2013; Supponen *et al.* 2016). The growth of the bubble and its interaction with the free surface (Mézel *et al.* 2009; Koukouvinis *et al.* 2016) results in jet formation. Visualization of bubble dynamics when the film is thin is experimentally challenging and not the focus of this article. We provide more details on the laser-induced bubble in appendix A and focus on the jet formation in the main body of the article.

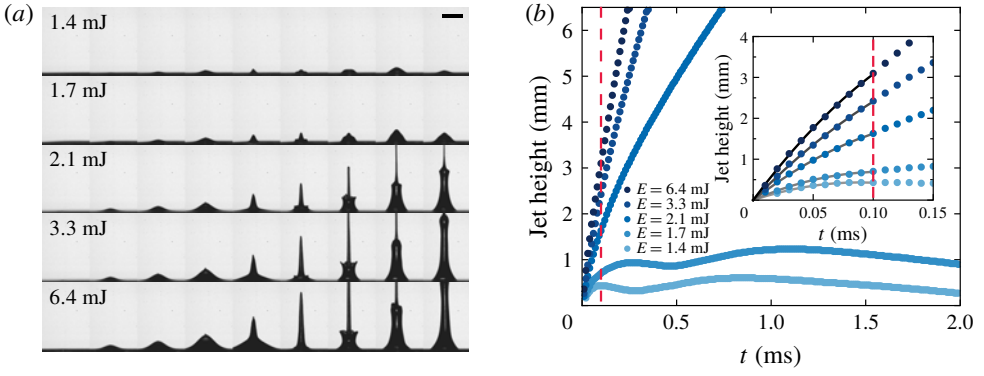

FIGURE 3. (Colour online) (*a*) Snapshots showing the evolution of the jet for sample 5 at $z_f = 0.5$ mm for various laser energies. The snapshots show the evolution of the jet for $t = 0.0$, 0.01, 0.02, 0.05, 0.1, 0.18, 0.33, 0.61, 1.1 and 2.0 ms. The scale bar corresponds to 2 mm. (*b*) The vertical extent of the jets versus time. The inset shows a zoom-in of the region for the early stage of ejection. The red dashed line demarcates the region $t \leqslant 0.1$ ms in which a quadratic fit is applied to extrapolate the jet velocity at $t = 0$. See the supplementary movies for the examples shown here.

When increasing the laser energy slightly above the plasma threshold, the interface only deforms to a small degree and forms a bump. Further increasing the laser energy results in jet formation. Depending on the experimental conditions, the jet might feature a crown, which forms due to the bubble dynamics inside the thin film (see appendix A). We measure the position of the jets as a function of time by high-speed imaging and subsequent image processing. Figure 3(*b*) shows the variation of the height of the jets shown in panel (*a*). When the laser energy is small, the bump relaxes, going through an oscillating behaviour. This is due to the propagation and interaction of the surface waves (see the supplementary movies, which are available at https://doi.org/10.1017/jfm.2019.731). However, the exact mechanisms involved in the propagation of these waves (surface tension, viscosity or elasticity) are not clear to us. When higher laser energies are applied, we only see the growth of the jets, in the time frame of our recordings.

Increasing the laser energy even further results in a faster jet. We find the jet velocity at small times by fitting the jet peak position by a second-order polynomial (for $t \leqslant 0.1$ ms) and extracting the slope at $t = 0$ (see the inset in figure 3*b*). We later compare these velocities for different conditions and use them to validate our model.

Figure 4 shows the jet evolution from sample 5 for different focal height z_f, with fixed laser energy at 2.1 mJ. Focusing on the free surface ($z_f = 0$) results in spray formation. This regime is different from the others since no bubble formation takes place inside the film. In fact, it is similar to what occurs in laser ablation of soft materials and liquids (Vogel & Venugopalan 2003; Thoroddsen *et al.* 2009). The high pressure of plasma leads to the formation of a sheet with a highly unstable front, which fragments into small droplets. The cylindrical sheet closes later and forms a thin jet that is unstable and disintegrates further in the process. By increasing the focal length z_f, we suppress the fragmentation and transit from sprays to jets of smaller height and velocity and eventually bumps.

Besides the laser energy, we also change the rheology of the samples. Figure 5 demonstrates the effect of rheology (yield stress τ_0 and nonlinear viscosity) on the

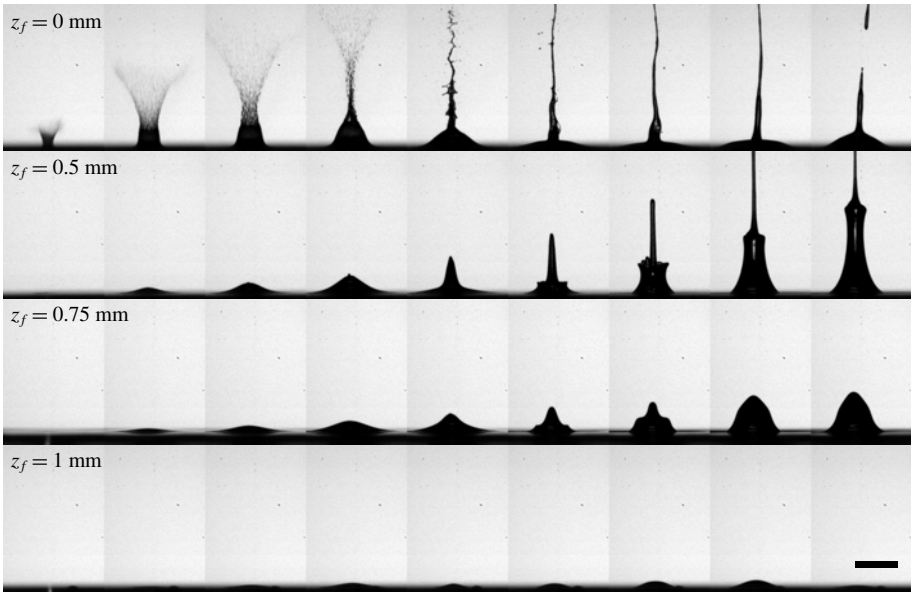

FIGURE 4. (*a*) Snapshots for increasing focal height at $t = 0$, 0.01, 0.02, 0.04, 0.1, 0.2, 0.4, 1 and 2 ms for $E = 2.1$ mJ and sample 5. The scale bar represents 2 mm. See the supplementary movies for the examples shown here.

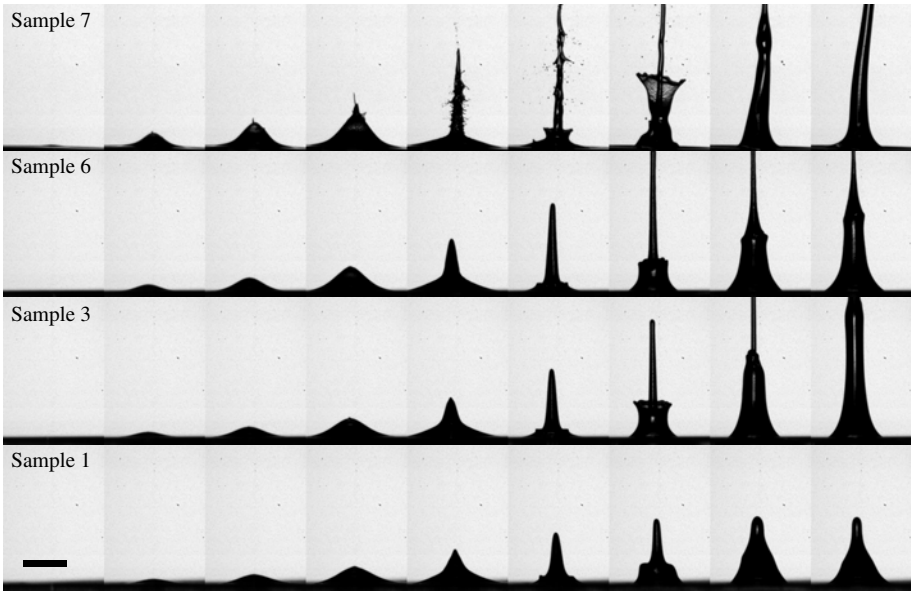

FIGURE 5. Snapshots for four different samples at $t = 0$, 0.01, 0.02, 0.04, 0.1, 0.2, 0.4, 1 and 2 ms where energy and focal height are fixed at $E = 5.1$ mJ, and $z_f = 0.5$ mm, respectively. Gels become stiffer from top to bottom (see figure 1). The scale bar represents 2 mm. See the supplementary movies for the examples shown here.

process of jet formation. In the experiments shown, the laser energy ($E = 5.1$ mJ) and focal height ($z_f = 0.5$) are fixed, and the gel stiffness varies (i.e. higher yield stress and apparent viscosity from top to bottom). It is shown that the ejection regimes can be significantly modified by increasing the effective viscosity. When the gel is very soft (sample 7) fragmentation occurs, producing small droplets. Additionally, the crown features a rim instability (fingers). Such instabilities, however, are suppressed by increasing the yield stress. Finally, the larger the yield stress, the shorter and slower the produced jet is.

As we have now shown, the jet morphologies vary from bumps to jets and sprays for different laser energies, focal heights and rheological parameters. Next, we will theoretically derive the jetting velocity and provide quantitative analysis to classify these regimes.

4. Theoretical analysis of the experimental results

4.1. *Characteristic jet velocity*

One of our main goals is to categorize the jetting regimes with non-dimensional groups to find optimal conditions for printing (a clean straight jet). To do so, a characteristic velocity is required that must be known prior to the specific experiments. Here, we provide a simple analysis to find such a velocity valid for small times, i.e. early on in the jetting process. We assume the absorbed energy contributes to optical breakdown (plasma formation) and subsequent bubble growth. Based on this assumption, the balance between the energies before and after the absorption reads

$$(I(t) - I_p)\,\mathrm{d}t = p(t)\,\mathrm{d}\mathcal{L}, \tag{4.1}$$

where I (measured in units of J m^{-2}) is the energy absorbed by the film per unit surface, I_p is the plasma threshold fluence, p is the pressure and $\mathcal{L}$ is the length of the cavity (see figure 2*b*). We assume that the cavity grows at a constant speed of $\mathrm{d}\mathcal{L}/\mathrm{d}t = p/(\rho c)$, where ρ and c are the density and the speed of sound, respectively (Fabbro *et al.* 1990; Asay & Shahinpoor 2012). If we also assume that the laser fluence remains constant during the pulse, we can find a characteristic pressure, namely

$$p_c = (I - I_p)^{1/2}(\rho c)^{1/2}. \tag{4.2}$$

This equation indeed gives the same order of magnitude (∼10 MPa) of the maximum pressures as reported in experiments with nanosecond lasers (Lauterborn & Vogel 2013). Here we assume $c = 1500$ m s^{-1}, as for water, since the polymer concentration is low and therefore its effect on the speed of sound is negligible (Povey 1997; Parker & Povey 2012).

Note that p_c is a constant characteristic pressure that gives a simple scaling with respect to the change of the laser energy. We will later elaborate on the simplifications made here. We now assume that p_c, over the characteristic time t_p, provides the momentum to a material cylinder above it. Hence, $p_c A t_p = A z_f \rho U_0$, where A is the area of the spot size of diameter D_s. We eventually find the characteristic velocity U_0 to be

$$U_0 = \beta t_p \left(\frac{c}{\rho}\right)^{1/2} \frac{(I - I_p)^{1/2}}{z_f}. \tag{4.3}$$

In (4.3), we have included an unknown parameter β that will be found later by fitting the experimental results.

We should emphasize that, by using a momentum balance like the one above, we make simplifications in five main ways. First, in reality, the pressure signal is time-dependent and strongly non-monotonic: it rapidly rises, reaches a maximum and then exponentially decays (see e.g. Lauterborn & Vogel 2013). Also, the lifetime of this pressure signal is much larger than the laser pulse duration (t_p) (Lauterborn & Vogel 2013; Wang *et al.* 2018). Therefore, a larger total momentum is expected. The rather large fitting parameter that we obtain later is mostly due to this assumption. Second, we assume that the reflection, scattering and transmission of the laser energy are negligible (as suggested by Vogel *et al.* (1999)). Third, upon the optical breakdown, an (almost spherical) bubble forms that pushes the fluid and the free surface above (see appendix A). This will create a more complicated flow field inside the films, in comparison to what is assumed here (Mézel *et al.* 2009; Brasz *et al.* 2015; Koukouvinis *et al.* 2016; Jalaal *et al.* 2019*b*). Fourth, we ignore the effects of temperature change inside the liquid, as it can influence the density and consequently the speed of sound. The latter is justified, as one expects that the temperature only changes within a few micrometres near the plasma point and also reaches the ambient temperature in a few microseconds (Vogel *et al.* 1999). Lastly, the rheological effects, such as elasticity, plasticity and viscosity, as well as the surface tension effects are assumed to be insignificant to our problem at small time. One can examine such an assertion through the corresponding time scales. The viscous time scale $t_{vis} = (z_f^2\rho/\mu)^{1/2} \approx 10^{-2}$ s, the gravitational time scale $t_g = (z_f/g)^{1/2} \approx 10^{-3}$ s and the capillary time scale $t_{cap} = (\rho z_f^3/\sigma) \approx 10^{-3}$ s are all much larger than the considered early stage time scale (which is the advection time scale, $t_{ad} = z_f/U_0 \approx 10^{-5}$ s). Similarly, the elastic relaxation time scale $t_{el} \approx (K/G_0')^{1/n} \approx 10^{-3}$ s is also much larger than the characteristic time scale of the early stage deformation. These time scales justify our inviscid assumption to find the early stage characteristic velocity (see e.g. Brasz *et al.* (2015) for a similar argument in the context of jet formation).

Despite the simplifications listed above, equation (4.3) successfully predicts the scaling laws previously seen in the laser–liquid interaction tests. The predicted power-law exponent $1/2$ is indeed close to the previously reported values in the context of droplet propulsion with a laser pulse (Basko, Novikov & Grushin 2015; Kurilovich *et al.* 2016). Also, the predicted $U_0 \sim z_f^{-1}$ dependence is the same as experimentally observed for jet formation in a capillary tube (Tagawa *et al.* 2012).

The application of (4.3) is restricted to the domain that excludes the boundaries. Focusing the laser close to the glass slide, i.e. $z_f/H \to 1$, results in solid ablation. This became evident when we found cracks in the glass slide. Moreover, equation (4.3) becomes singular when $z_f/H \to 0$ (i.e. focusing close to the free surface) and obviously can then no longer hold. In our experiments, the divergence of the velocity appears as an explosive splash of the film in the sheet opening and splash regime (see figure 4). Figure 6(*a*) shows the variation of the early jet velocities U_0 for different samples at different laser energies. As expected, we do not observe any significant effect of the rheological properties on U_0, meaning that inertia is dominating any possible elastoviscoplastic effects. Moreover, the value of the plasma threshold I_p also remains insensitive to the concentration of polymers. The predicted power law (4.3) is in good agreement with the trends observed in the experiments $U_0 \propto (I - I_p)^{1/2}$. Fitting through the mean values of the data (see figure 6*a*), we find $\beta \approx 174$.

We then compare the model with experiments of samples at different focal heights. An example is shown in figure 6(*b*), where $\beta = 174$ is fixed. The results of the model

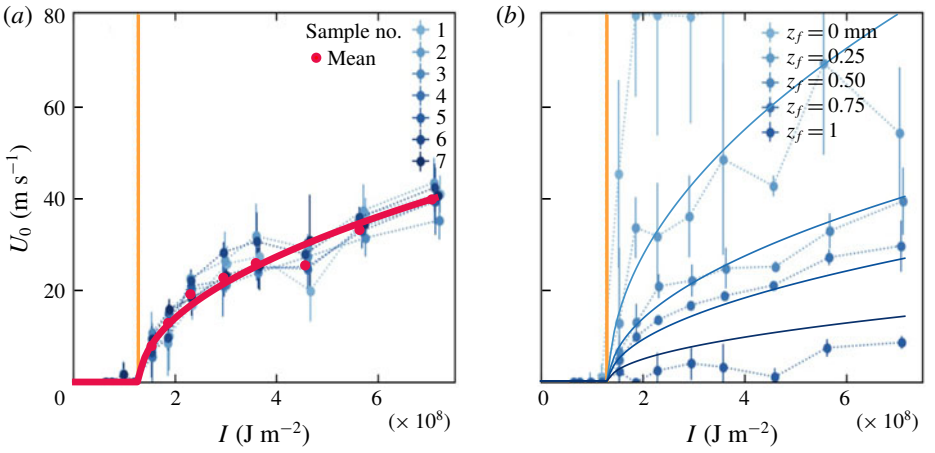

FIGURE 6. (Colour online) Jet velocity at different laser fluences for (*a*) different samples, but fixed $z_f = 0.5$, and (*b*) sample 5, at different focal heights, z_f (see legend). The yellow vertical dashed lines denote $I = I_p$. In both panels (*a*) and (*b*), the solid lines are from (4.3) with $\beta = 174$. Error bars denote the standard deviation from multiple experiments.

are in good agreement, implying that $U_0 \sim z_f^{-1}$ is satisfactory. Note that we cannot compare the model for $z_f = 0$, as then $U_0 \to \infty$. Furthermore, we use an average value for the sound speed c for the case of $z_f = H$, as the plasma forms at the interface of the glass and the gel. Nonetheless, the difference between the experiments and theory remains large, which might be because of additional complexities due to the glass ablation, as explained above.

4.2. *Phase diagram and non-dimensional groups*

We identify six different regimes of jets from our experiments, namely a bump regime (the jet is shallow with a maximum aspect ratio of less than unity), a jet regime (when a long straight jet with no significant crown forms), a crown jet regime (where a crown follows the straight jet), an unstable crown jet regime (where the edge of the crown becomes unstable and forms fingers), a fragmented jet regime (where the jet disintegrates into smaller droplets in the early stage of formation), and finally a spray regime (where the sheet opens, forms many small droplets and the sheet closure results in even more fragmentation). In figure 7, we show examples of these regimes and the dimensional phase space in these control parameters: laser energy, yield stress (gel stiffness) and focal height. When $z_f = 0$, we only observe sprays. As a trend, increasing the gel stiffness and/or the focal height, as well as decreasing the laser energy, results in a less developed morphology.

In general, inertial forces due to the laser pulse compete with capillary, viscous and plastic forces to define the dynamics and morphology of the jets. With the characteristic velocity found above (4.3), we define the following two non-dimensional groups:

$$We = \frac{\rho U_0^2 z_f}{\sigma} \quad \text{and} \quad Re = \frac{\rho U_0^2}{K(U_0/z_f)^n + \tau_0}. \tag{4.4a,b}$$

The Weber number We compares the inertial stresses and capillary pressure. The Reynolds number Re compares the inertial stress and the total internal stress. The

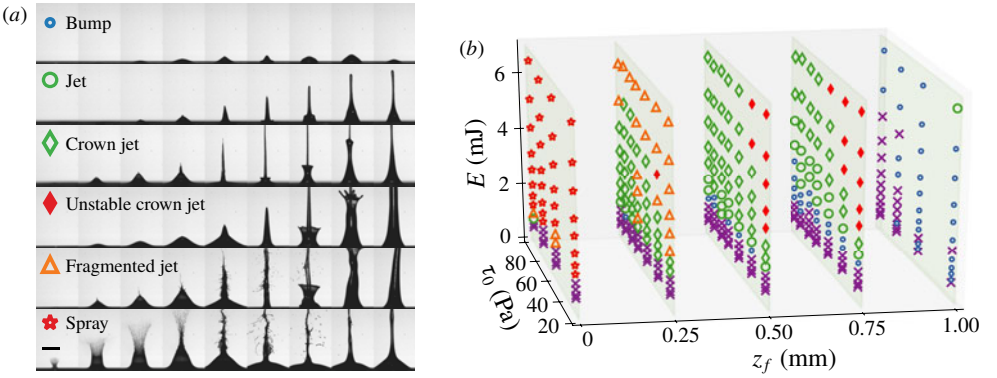

FIGURE 7. (Colour online) (*a*) Examples of the jetting regimes observed in the experiments. The experimental conditions from top to bottom are: bump, $E = 2.1$ mJ, $z_f/H = 0.75$, sample no. 2; jet, $E = 2.7$ mJ, $z_f/H = 0.5$, sample no. 1; jet with a crown, $E = 2.6$ mJ, $z_f/H = 0.25$, sample no. 5; jet with an unstable crown, $E = 6.3$ mJ, $z_f/H = 0.75$, sample no. 6; fragmented jet, $E = 6.4$ mJ, $z_f/H = 0.25$, sample no. 6; spray, $E = 6.3$ mJ, $z_f/H = 0$, sample no. 5. (*b*) Three-dimensional phase space of the regimes for different laser energy E, yield stress τ_0 and focal height z_f. Crosses denote the experiments in which no deformation was detected. See the supplementary material for movies for the examples shown here and the 3-D animation of the phase space.

latter contains two parts due to the shear thinning (with a characteristic shear rate of U_0/z_f) and the plastic viscosities. A Reynolds number of this type has previously been used in the context of viscoplastic droplets (Blackwell *et al.* 2015; Jalaal, Kemper & Lohse 2019*a*) and other configurations (Thompson & Soares 2016). Note that by using such a non-dimensional group, we assume that the yield stress only contributes via the plastic viscosity. We also ignore the effect of the film thickness H and assume that the height of the laser focus z_f is the only important length scale.

Figure 8 shows the non-dimensional phase diagram. Note that, in figure 8, we do not include data for $z_f/H = 1$, due to the complexities from the glass ablation, nor those for $z_f/H = 0$, as they only result in spray formation and our theoretical velocity (therefore, both Re and We) diverges in that asymptotic limit. At relatively low Weber and Reynolds numbers, the inertial effects are overwhelmed by the viscous and capillary forces and only a bump forms. Increasing the Reynolds and Weber numbers results in jets, crown formation, unstable crowns and eventually fragmentation.

We inspect the non-dimensional map using two other non-dimensional numbers common in printing technologies: the capillary number $Ca = We/Re$ and the Ohnesorge number $Oh = We^{1/2}/Re$. Our experimental data are bounded within the two bounds of $Ca = 1$ and $Ca = 0.1$. This is a consequence of the range of experimental parameters employed here. Using (4.3), for a given gel, one finds $Ca \sim (I - I_0)^{n/2} z_f^{1-2n}$. For our gels, $2n \approx 1$; therefore, Ca is a function of only the laser energy. For the range of laser energy we used here, $(I - I_0)^{n/2}$ remains close to unity. Therefore, Ca is almost constant for a given gel. Therefore the straight line envelopes show up. The dashed grey lines in figure 8 denote these bounds.

The Ohnesorge number (in its simple form for Newtonian liquids) is commonly used in inkjet printing application to find the regimes in which one single droplet forms (typically $0.1 < Oh < 1$). If Oh is large, then the material is too viscous to be

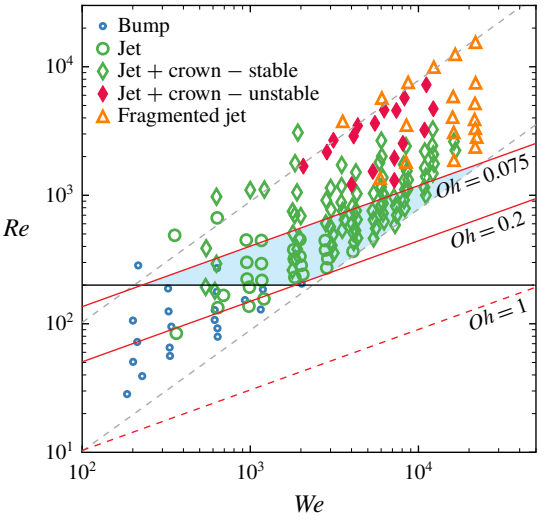

FIGURE 8. (Colour online) Phase space in terms of Reynolds and Weber numbers. The dashed grey lines correspond to $Ca = 0.1$ and 1. The horizontal black line shows $Re = 200$. The shaded region highlights the optimal printing condition with LIFT.

printed; and if $Oh \leqslant 1$, then multiple droplets might form (Derby 2010; McKinley & Renardy 2011). We use the same analogy here to find the optimal regime of printing, where a straight jet forms. All the experiments shown in figure 8 feature $Oh < 1$ (a common criterion in inkjet printing noted by the red dashed line in figure 8). For the range of $0.075 < Oh < 0.2$, we obtain jet morphologies that can be used for LIFT printing. Within this range, the proper balance between total viscosity and inertia does not allow for fragmentation or significant crown formation. We also introduce another criterion of $Re > 200$ to exclude bumps. When Re is smaller than this critical value, the viscous dissipation is strong enough to resist jet formation. The shaded region in figure 8 shows the region we suggest for optimal printing with LIFT.

5. Conclusions and outlook

In this paper, we experimentally studied the LIFT of viscoplastic materials, in which the ejection is driven by direct absorption of the laser. Several parameters, such as the laser energy, focal height and the rheology of the material, determine the shape of the jet, which can vary from bumps, jets with stable or unstable crowns, and fragmented jets, to sprays. In most applications, a non-fragmenting straight jet is desirable. To look for suitable conditions, we reduce the parameter space to two non-dimensional groups, namely the Reynolds and Weber numbers, which include rheological properties such as the nonlinear shear dependence and the yield stress.

Our dimensional analysis for the current LIFT set-up suggests operating conditions that satisfy the two conditions of $0.075 < Oh < 0.2$ and $Re > 200$. Outside these ranges, the viscous dissipation (due to the shear-thinning and plastic viscosities) is either too large to avoid jetting or too small to make a stable straight jet. We note that the conditions above are for jet formation only. Depending on the technical details of printing, additional conditions can be introduced for optimal printing. For instance, one should avoid splashing when droplets are deposited on the surface (Derby 2010).

Our study has direct applications in printing 2-D or 3-D structures with soft materials, featuring viscoplastic properties. In particular, it provides information for printing flexible electronics with metallic pastes and hydrogels in bio-printing. Moreover, the non-dimensional numbers used here can be obtained prior to printing, knowing the properties of the laser pulse and the material (ink). The only other requirement is to find a correct characteristic velocity. Here, we use an energy balance argument to obtain the latter. The type of analysis provided here can, in its general form, be used for any LIFT configuration or any other printing system that utilizes jets of inelastic generalized Newtonian fluids. For instance, for a blister-actuated LIFT (e.g. Turkoz *et al.* 2018*b*), one only needs to use a different characteristic velocity related to the deformation of the blister.

We finally note that inks, such as silver pastes, can feature even more complex rheological properties. Moreover, the detailed mechanisms of optical absorption and breakdown can vary. A first attempt to study such a more complicated system could be to test LIFT for a granular suspension with Newtonian or non-Newtonian suspending fluids (Guazzelli & Pouliquen 2018).

Acknowledgements

We would like to thank B. Benschop, M. Bos and G.-W. Bruggert for their technical assistance. The authors thank C. Seyfert, A. Klein, G. Arutinov, D. van der Meer and A. Prosperetti for useful discussions. This work was funded by the Netherlands Organisation for Scientific Research (NWO).

Supplementary movies

Supplementary movies are available at https://doi.org/10.1017/jfm.2019.731.

Appendix A. Bubble dynamics

To elaborate more on the underlying fluid mechanics of a LIFT process, we performed model experiments with thick films. In contrast to the main experiments, where $H = 1$ mm, here we are able to visualize the dynamics of the bubble as well as the jet formation. Instead of a thin film, we fill a container and focus the laser close to the interface. Such an experiment is not a realistic mimic of a common LIFT system with a thin ink layer (it is instead close to the so-called film-free LIFT, see e.g. Piqué *et al.* (2018)). Nonetheless, it provides useful information on the underlying fluid mechanics of the problem. Figure 9 shows an example of jet formation for a water film with $H = 4$ mm and $z_f = 1$ mm.

The process is as follows. Optical breakdown results in plasma formation (shown by the black arrow in figure 9*a*) and as a consequence a bubble forms inside the liquid (figure 9*b*) that contains vapour (see Jalaal *et al.* (2019*b*) for more information on the early stage of LIFT). The bubble grows, initiating the liquid jet (figure 9*c*) and then collapses under hydrostatic pressure (shown by blue arrows in figure 9*d*). Meanwhile, the liquid jet is extending vertically (shown by the orange arrow in figure 9*d*). During the bubble collapse a downward micro-jet forms (due to gravity, the presence of the wall and the free surface). This micro-jet impacts on the bottom of the bubble (see Supponen *et al.* (2016) for details), resulting in a complex toroidal shape of secondary bubbles (figure 9*f*). The formation of the crown seems to be highly connected to the second growth of the bubble, when it pushes the perimeter around the jet and

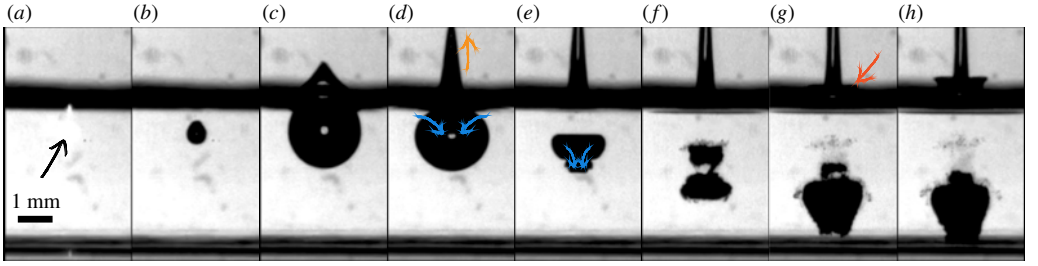

FIGURE 9. (Colour online) Process of bubble, jet and crown formation in a thick film. Snapshots correspond to (*a*) $t = 0$ μs, (*b*) $t = 5$ μs, (*c*) $t = 125$ μs, (*d*) $t = 250$ μs, (*e*) $t = 350$ μs, (*f*) $t = 450$ μs, (*g*) $t = 575$ μs and (*h*) $t = 625$ μs.

forms a crown. A complete explanation of the crown dynamics, however, requires more experiments and analysis.

The process explained above is expected to be more complicated when the film thickness becomes thin, as the interaction between the bubble, the free surface and the bottom wall is expected to be more pronounced. Exploring such a system requires more sophisticated visualization tools.

Appendix B. Elasticity

Our analysis does not include the effects of elasticity. Here, we briefly justify our assumption and note the possible effects of elasticity. Instead of (2.1), one might use a more complicated constitutive model that features viscoelasticity after yielding. An example of an elastoviscoplastic constitutive model is as follows (Luu & Forterre 2009; Saramito 2009; Fraggedakis, Dimakopoulos & Tsamopoulos 2016):

$$\tau = G'\gamma_{el}:$$

$$\frac{\mathrm{d}\gamma_{el}}{\mathrm{d}t} = \dot{\gamma} \quad \text{if} \quad |\gamma_{el}| < \gamma_c, \tag{B 1}$$

$$\frac{\mathrm{d}\gamma_{el}}{\mathrm{d}t} = \dot{\gamma} - \frac{1}{\lambda}\frac{|\gamma_{el}| - \gamma_c}{|\gamma_{el}|}\gamma_{el} \quad \text{if} \quad |\gamma_{el}| > \gamma_c, \tag{B 2}$$

where γ_{el} is the reversible elastic deformation and γ_c is the yield strain. The model above, similar to (2.1), assumes that the material is a linear elastic solid before yielding. After yielding, however, the rate of deformation includes an additional creep term, featuring a relaxation time $\lambda \approx (K/G')^{1/n}$. For a fast transient experiment, looking at equation (B 2), one might expect that, if the deformation time scale is much shorter than the relaxation time scale, the response is always dominated by elasticity, even after yielding. An argument of this type has been made by Luu & Forterre (2009) in the context of the impact of yield-stress droplets. In making such an argument, one should, however, consider the dependence of elastic properties on deformation history. Our rheological measurements (see figure 1) show clear non-constant elastic properties above the yield stress (or yield strain of $\gamma_c \approx 25\,\%$), as the magnitude of the elastic modulus G' drops orders of magnitude when deformation is large. Therefore, for the time window of our study, we expect that the viscoplastic response is dominating. One should note that, much later in the process, when the jet, droplets or the crater are relaxing, the elastic effects can be important. Therefore,

to investigate these processes, we should include the effects of elasticity, using dimensionless numbers such as the Deborah number (Luu & Forterre 2009; Turkoz *et al.* 2018*b*).

REFERENCES

ANDO, K., LIU, A.-Q. & OHL, C.-D. 2012 Homogeneous nucleation in water in microfluidic channels. *Phys. Rev. Lett.* **109** (4), 044501.

ASAY, J. R. & SHAHINPOOR, M. 2012 *High-Pressure Shock Compression of Solids*. Springer Science & Business Media.

BALMFORTH, N. J., FRIGAARD, I. A. & OVARLEZ, G. 2014 Yielding to stress: recent developments in viscoplastic fluid mechanics. *Annu. Rev. Fluid Mech.* **46**, 121–146.

BASKO, M. M., NOVIKOV, V. G. & GRUSHIN, A. S. 2015 On the structure of quasi-stationary laser ablation fronts in strongly radiating plasmas. *Phys. Plasmas* **22** (5), 053111.

BLACKWELL, B. C., DEETJEN, M. E., GAUDIO, J. E. & EWOLDT, R. H. 2015 Sticking and splashing in yield-stress fluid drop impacts on coated surfaces. *Phys. Fluids* **27** (4), 043101.

BONN, D., DENN, M. M., BERTHIER, L., DIVOUX, T. & MANNEVILLE, S. 2017 Yield stress materials in soft condensed matter. *Rev. Mod. Phys.* **89** (3), 035005.

BOUJLEL, J. & COUSSOT, P. 2013 Measuring the surface tension of yield stress fluids. *Soft Matt.* **9** (25), 5898–5908.

BRASZ, C. F., ARNOLD, C. B., STONE, H. A. & LISTER, J. R. 2015 Early-time free-surface flow driven by a deforming boundary. *J. Fluid Mech.* **767**, 811–841.

COLINA, M., DUOCASTELLA, M., FERNÁNDEZ-PRADAS, J. M., SERRA, P. & MORENZA, J. L. 2006 Laser-induced forward transfer of liquids: study of the droplet ejection process. *J. Appl. Phys.* **99** (8), 084909.

DERBY, B. 2010 Inkjet printing of functional and structural materials: fluid property requirements, feature stability, and resolution. *Annu. Rev. Mater. Res.* **40**, 395–414.

DINKGREVE, M., PAREDES, J., DENN, M. M. & BONN, D. 2016 On different ways of measuring the yield stress. *J. Non-Newtonian Fluid Mech.* **238**, 233–241.

FABBRO, R., FOURNIER, J., BALLARD, P., DEVAUX, D. & VIRMONT, J. 1990 Physical study of laser-produced plasma in confined geometry. *J. Appl. Phys.* **68** (2), 775–784.

FRAGGEDAKIS, D., DIMAKOPOULOS, Y. & TSAMOPOULOS, J. 2016 Yielding the yield stress analysis: a thorough comparison of recently proposed elasto-visco-plastic (evp) fluid models. *J. Non-Newtonian Fluid Mech.* **236**, 104–122.

GÉRAUD, B., JØRGENSEN, L., YBERT, C., DELANOË-AYARI, H. & BARENTIN, C. 2017 Structural and cooperative length scales in polymer gels. *Eur. Phys. J.* E **40** (1), 5.

GUAZZELLI, É. & POULIQUEN, O. 2018 Rheology of dense granular suspensions. *J. Fluid Mech.* **852**, P1.

HOPKINS, C. C. & DE BRUYN, J. R. 2019 Gelation and long-time relaxation of aqueous solutions of pluronic f127. *J. Rheol.* **63** (1), 191–201.

HU, R. Y. Z., WANG, A. T. A. & HARTNETT, J. P. 1991 Surface tension measurement of aqueous polymer solutions. *Exp. Therm. Fluid Sci.* **4** (6), 723–729.

ISHIGURO, S. & HARTNETT, J. P. 1992 Surface tension of aqueous polymer solutions. *Intl Commun. Heat Mass Transfer* **19** (2), 285–295.

JALAAL, M., BALMFORTH, N. J. & STOEBER, B. 2015 Slip of spreading viscoplastic droplets. *Langmuir* **31** (44), 12071–12075.

JALAAL, M., COTTRELL, G., BALMFORTH, N. & STOEBER, B. 2017 On the rheology of pluronic f127 aqueous solutions. *J. Rheol.* **61** (1), 139–146.

JALAAL, M., KEMPER, D. & LOHSE, D. 2019*a* Viscoplastic water entry. *J. Fluid Mech.*; (to appear).

JALAAL, M., LI, S., KLEIN SCHAARSBERG, M., QIN, Y. & LOHSE, D. 2019*b* Destructive mechanisms in laser induced forward transfer. *Appl. Phys. Lett.* **114** (21), 213703.

JØRGENSEN, L., LE MERRER, M., DELANOË-AYARI, H. & BARENTIN, C. 2015 Yield stress and elasticity influence on surface tension measurements. *Soft Matt.* **11** (25), 5111–5121.

KATGERT, G., LATKA, A., MÖBIUS, M. E. & VAN HECKE, M. 2009 Flow in linearly sheared two-dimensional foams: from bubble to bulk scale. *Phys. Rev.* E **79** (6), 066318.

KENNEDY, P. K., HAMMER, D. X. & ROCKWELL, B. A. 1997 Laser-induced breakdown in aqueous media. *Prog. Quantum Electron.* **21** (3), 155–248.

KIM, J.-Y., SONG, J.-Y., LEE, E.-J. & PARK, S.-K. 2003 Rheological properties and microstructures of carbopol gel network system. *Colloid Polym. Sci.* **281** (7), 614–623.

KOUKOUVINIS, P., GAVAISES, M., SUPPONEN, O. & FARHAT, M. 2016 Simulation of bubble expansion and collapse in the vicinity of a free surface. *Phys. Fluids* **28** (5), 052103.

KURILOVICH, D., KLEIN, A. L., TORRETTI, F., LASSISE, A., HOEKSTRA, R., UBACHS, W., GELDERBLOM, H. & VERSOLATO, O. O. 2016 Plasma propulsion of a metallic microdroplet and its deformation upon laser impact. *Phys. Rev.* A **6** (1), 014018.

LAUTERBORN, W. & VOGEL, A. 2013 Shock wave emission by laser generated bubbles. In *Bubble Dynamics and Shock Waves*, pp. 67–103. Springer.

LIDON, P., VILLA, L. & MANNEVILLE, S. 2017 Power-law creep and residual stresses in a carbopol gel. *Rheol. Acta* **56** (3), 307–323.

LUU, L.-H. & FORTERRE, Y. 2009 Drop impact of yield-stress fluids. *J. Fluid Mech.* **632**, 301–327.

MANGLIK, R. M., WASEKAR, V. M. & ZHANG, J. 2001 Dynamic and equilibrium surface tension of aqueous surfactant and polymeric solutions. *Exp. Therm. Fluid Sci.* **25** (1–2), 55–64.

MCKINLEY, G. H. & RENARDY, M. 2011 Wolfgang von ohnesorge. *Phys. Fluids* **23** (12), 127101.

MEEKER, S. P., BONNECAZE, R. T. & CLOITRE, M. 2004 Slip and flow in soft particle pastes. *Phys. Rev. Lett.* **92** (19), 198302.

MÉZEL, C., HALLO, L., SOUQUET, A., BREIL, J., HÉBERT, D. & GUILLEMOT, F. 2009 Self-consistent modeling of jet formation process in the nanosecond laser pulse regime. *Phys. Plasmas* **16** (12), 123112.

MUNOZ-MARTIN, D., BRASZ, C. F., CHEN, Y., MORALES, M., ARNOLD, C. B. & MOLPECERES, C. 2016 Laser-induced forward transfer of high-viscosity silver pastes. *Appl. Surf. Sci.* **366**, 389–396.

OBRESCHKOW, D., TINGUELY, M., DORSAZ, N., KOBEL, P., DE BOSSET, A. & FARHAT, M. 2013 The quest for the most spherical bubble: experimental setup and data overview. *Exp. Fluids* **54** (4), 1503.

PARKER, N. G. & POVEY, M. J. W. 2012 Ultrasonic study of the gelation of gelatin: phase diagram, hysteresis and kinetics. *Food Hydrocolloids* **26** (1), 99–107.

PIQUÉ, A., SERRA, P., SURDO, S., DIASPRO, A. & DUOCASTELLA, M. 2018 Film-Free LIFT (FF-LIFT). In *Laser Printing of Functional Materials* (ed. A. Piqué & P. Serra). doi:10.1002/9783527805105.ch6.

POHL, R., VISSER, C. W., RÖMER, G.-W., LOHSE, D., SUN, C., HUIS, B. & OTHERS 2015 Ejection regimes in picosecond laser-induced forward transfer of metals. *Phys. Rev.* A **3** (2), 024001.

POVEY, M. J. W. 1997 *Ultrasonic Techniques for Fluids Characterization*. Elsevier.

ROBERTS, G. P. & BARNES, H. A. 2001 New measurements of the flow-curves for carbopol dispersions without slip artefacts. *Rheol. Acta* **40** (5), 499–503.

SARAMITO, P. 2009 A new elastoviscoplastic model based on the Herschel–Bulkley viscoplastic model. *J. Non-Newtonian Fluid Mech.* **158** (1–3), 154–161.

SERRA, P. & PIQUÉ, A. 2018 Laser-induced forward transfer: fundamentals and applications. In *Advanced Materials Technologies*, p. 1800099.

SUPPONEN, O., OBRESCHKOW, D., TINGUELY, M., KOBEL, P., DORSAZ, N. & FARHAT, M. 2016 Scaling laws for jets of single cavitation bubbles. *J. Fluid Mech.* **802**, 263–293.

TAGAWA, Y., OUDALOV, N., VISSER, C. W., PETERS, I. R., VAN DER MEER, D., SUN, C., PROSPERETTI, A. & LOHSE, D. 2012 Highly focused supersonic microjets. *Phys. Rev. X* **2** (3), 031002.

THOMPSON, R. L. & SOARES, E. J. 2016 Viscoplastic dimensionless numbers. *J. Non-Newtonian Fluid Mech.* **238**, 57–64.

THORODDSEN, S. T., TAKEHARA, K., ETOH, T. G. & OHL, C.-D. 2009 Spray and microjets produced by focusing a laser pulse into a hemispherical drop. *Phys. Fluids* **21** (11), 112101.

TURKOZ, E., FARDEL, R. & ARNOLD, C. B. 2018*a* Advances in blister-actuated laser-induced forward transfer (ba-lift). In *Laser Printing of Functional Materials: 3D Microfabrication, Electronics and Biomedicine*, pp. 91–121.

TURKOZ, E., PERAZZO, A., KIM, H., STONE, H. A. & ARNOLD, C. B. 2018*b* Impulsively induced jets from viscoelastic films for high-resolution printing. *Phys. Rev. Lett.* **120** (7), 074501.

VISSER, C. W., POHL, R., SUN, C., RÖMER, G.-W., HUIS IN 'T VELD, B. & LOHSE, D. 2015 Toward 3D printing of pure metals by laser-induced forward transfer. *Adv. Mater.* **27** (27), 4087–4092.

VOGEL, A., NAHEN, K., THEISEN, D. & NOACK, J. 1996 Plasma formation in water by picosecond and nanosecond nd: Yag laser pulses. I. Optical breakdown at threshold and superthreshold irradiance. *IEEE J. Selected Topics Quantum Electron.* **2** (4), 847–860.

VOGEL, A., NOACK, J., NAHEN, K., THEISEN, D., BUSCH, S., PARLITZ, U., HAMMER, D. X., NOOJIN, G. D., ROCKWELL, B. A. & BIRNGRUBER, R. 1999 Energy balance of optical breakdown in water at nanosecond to femtosecond time scales. *Appl. Phys.* B **68** (2), 271–280.

VOGEL, A. & VENUGOPALAN, V. 2003 Mechanisms of pulsed laser ablation of biological tissues. *Chem. Rev.* **103** (2), 577–644.

WANG, J., AUYEUNG, R. C. Y., KIM, H., CHARIPAR, N. A. & PIQUÉ, A. 2010 Three-dimensional printing of interconnects by laser direct-write of silver nanopastes. *Adv. Mater.* **22** (40), 4462–4466.

WANG, Y., ZAYTSEV, M. E., LAJOINIE, G., EIJKEL, J. C. T., VAN DEN BERG, A., VERSLUIS, M., WECKHUYSEN, B. M., ZHANG, X., ZANDVLIET, H. J. W. & LOHSE, D. 2018 Giant and explosive plasmonic bubbles by delayed nucleation. *Proc. Natl Acad. Sci.* **115** (30), 7676–7681.

XIONG, R., ZHANG, Z., CHAI, W., HUANG, Y. & CHRISEY, D. B. 2015 Freeform drop-on-demand laser printing of 3D alginate and cellular constructs. *Biofabrication* **7** (4), 045011.

ZENOU, M., SA'AR, A. & KOTLER, Z. 2015 Laser transfer of metals and metal alloys for digital microfabrication of 3D objects. *Small* **11** (33), 4082–4089.